Geophysical Research Letters

RESEARCH LETTER
10.1029/2021GL092986

Key Points:

- Rietveld texture analysis of low-grade metamorphic serpentinites
- Anisotropy increase with deformation intensity
- Seismic anisotropy of shear zones in oceanic serpentinites

Supporting Information:

Supporting Information may be found in the online version of this article.

Correspondence to:

R. Kuehn,
rebecca.kuehn@geo.uni-halle.de

Citation:

Kuehn, R., Behrmann, J. H., Stipp, M., Kilian, R., & Leiss, B. (2021). Deformation, CPO, and elastic anisotropy in low-grade metamorphic serpentinites, Atlantis Massif oceanic core complex. *Geophysical Research Letters*, *48*, e2021GL092986. https://doi.org/10.1029/2021GL092986

Received 15 FEB 2021
Accepted 8 APR 2021

Deformation, CPO, and Elastic Anisotropy in Low-Grade Metamorphic Serpentinites, Atlantis Massif Oceanic Core Complex

R. Kuehn[1], J. H. Behrmann[2], M. Stipp[1], R. Kilian[1], and B. Leiss[3]

[1]Institute of Geosciences and Geography, Martin-Luther-University Halle, Halle (Saale), Germany, [2]GEOMAR Helmholtz Centre for Ocean Research Kiel, Marine Geodynamics, Kiel, Germany, [3]Department of Structural Geology and Geodynamics, Geoscience Center of the Georg-August-Universität Göttingen, Göttingen, Germany

Abstract Crystallographic preferred orientation (CPO) and the associated seismic anisotropy of serpentinites are important factors for the understanding of tectonic settings involving hydrated Earth´s mantle, for example, at slow-spreading mid-ocean ridges. CPO of lizardite and magnetite in low-grade metamorphic serpentinites from the Atlantis Massif oceanic core complex (Mid-Atlantic Ridge, 30°N) were determined using synchrotron high energy X-ray diffraction in combination with Rietveld texture analysis. Serpentinite mesh structures show weak CPO while deformed samples show a single (0001) maximum perpendicular to the foliation. Seismic anisotropies calculated from CPO show up to >11% anisotropy for compressional waves (*Vp*) and shear wave splitting up to 0.38 km/s in the deformed samples. This indicates that deformation in shear zones controls elastic anisotropy and highlights its importance in defining the seismic signature of hydrated upper mantle.

Plain Language Summary The easy deformability of serpentinites is important in settings where tectonic plates move relative to each other. Serpentinites form when rocks which belong to the Earth's mantle get in contact with water and react. As the distribution of serpentinites within the oceanic lithosphere cannot be determined from direct observations, we can only refer to seismic data. In crystals, physical properties such as the velocity of seismic waves can vary with direction. The internal structure of a rock, a multi-crystal material, hence provides a complex function of seismic wave velocities depending on the arrangement of these crystals. Alignment of the crystals is usually thought to be strengthened by deformation. At the Atlantis Massif (30°N, Mid-Atlantic ridge), serpentinites were sampled by scientific ocean drilling. We analyzed the arrangement of the crystals using focused X-rays and can distinguish different microstructures originating from different intensities of deformation. The spatial orientation of the crystals was analyzed using high-energy X-ray diffraction. We find different states of ordering of the crystals which we associate with different states of deformation. From those data, we can compute the seismic properties of such rocks. The findings can help to detect zones of strong deformation in the Earth's Upper Mantle.

1. Introduction

Serpentinites are of great importance for the understanding of lithosphere dynamics and active plate tectonic processes (cf., Guillot et al., 2015). They form by hydration of mantle peridotite and occur at slow-spreading mid-ocean ridges (e.g., Aumento & Loubat, 1971), in lithospheric mantle wedges above descending slabs in subduction zones (e.g., Jung, 2011; Solarino et al., 2018; Zhao et al., 2020), in ocean-continent transition zones (e.g., Lau et al., 2006; Sutra et al., 2013) and continental strike-slip zones (e.g., Moore & Rymer, 2007).

In the temperature range of <300°C–400°C (Evans, 2004), as present at oceanic spreading ridges and transforms, lizardite, the flat-stacked serpentine mineral polymorph, and chrysotile, the fibrous serpentine polymorph, are dominantly formed from olivine and pyroxene. A mesh microstructure, typical for low-grade metamorphic serpentinites, is formed by polycrystalline pseudomorphs of serpentine after olivine when deformation is absent or low (cf., Viti et al., 2018). Serpentinization usually starts at grain boundaries and cracks forming mesh rims of serpentine, mostly composed of lizardite platelets (e.g., Wicks & Whittaker, 1977) stacked in columns normal to the olivine reaction surface (Boudier et al., 2010). Mesh rims are often traced by fine-grained magnetite, if present. Mesh cores can be of fine-grained, optically isotropic

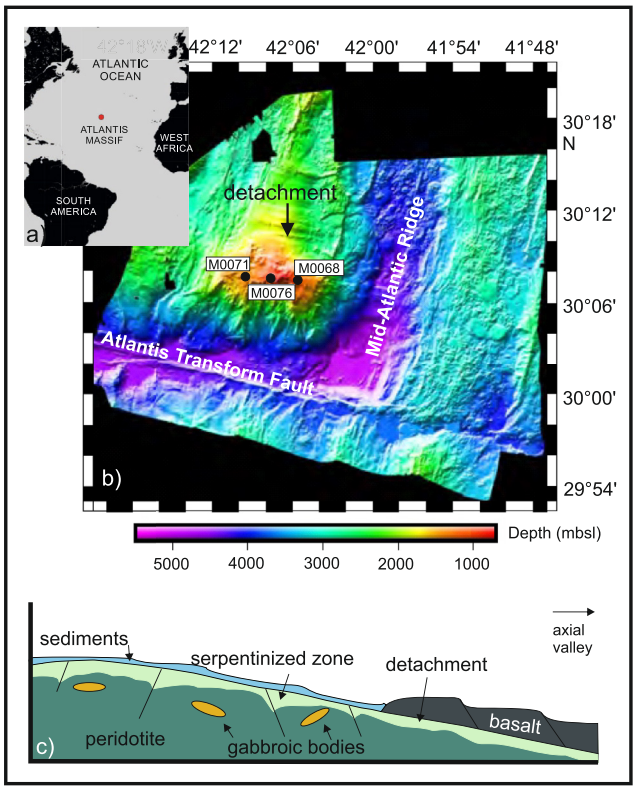

Figure 1. (a) Location of Atlantis Massif along the Mid-Atlantic Ridge (MAR). (b) Bathymetric map of the Atlantis Massif Oceanic Core Complex. Black circles mark drill locations of IODP Expedition 357 from where our samples originate (modified from Früh-Green et al., 2017). (c) Sketched section of the southern Atlantis Massif (redrawn after Boschi et al., 2006), showing the supposed distribution of serpentinites.

serpentine of low crystallinity. Bastite, a pseudomorphic serpentine aggregate after pyroxene, can consist of fine-grained lizardite and chrysotile (Wicks & Whittaker, 1977).

Serpentinization fundamentally modifies peridotite rheology, and results in a reduction of strength (Escartin et al., 2001; Raleigh & Paterson, 1965). This plays an important role for strain localization in the tectonic settings mentioned above. In the brittle regime shear fractures and ruptures are observed parallel as well as at high angles to the (001) planes (Escartin et al., 1997). Dominant deformation mechanisms of lizardite as deduced from deformation experiments in the viscous regime are slip on (001) and kinking (Amiguet et al., 2012, 2014). All deformation mechanisms can contribute to the development of a crystallographic preferred orientation (CPO) or texture and induce a stronger elastic anisotropy.

Given the high elastic anisotropy of serpentine minerals (Auzende et al., 2006; Bezacier et al., 2010; Tsuchiya, 2013), CPO development has potentially large effects on bulk rock elastic properties of hydrated oceanic mantle rocks. The change in elastic properties applies not only to average acoustic velocity, but also to the anisotropy of compressive (P) and shear (S) wave velocities. This is important for the correct interpretation of seismic and seismological data.

CPO analysis of low-grade metamorphic serpentinites was so far mostly restricted to TEM (transmission electron microscopy) observations, which are spatially very limited. Here, we present CPO data and the calculated elastic anisotropies obtained from large samples of variably deformed serpentinites from the Atlantis Massif using high-energy synchrotron X-ray diffraction measurements in combination with Rietveld refinement.

2. Geological Setting and Samples

The Atlantis Massif, located at 30°N at the Mid-Atlantic Ridge (MAR), is a 1.5–2 Myr old (Blackman et al., 1998, 2002), domal structure bounded to the south by the Atlantis Transform Fault and to the East by the MAR median valley (Figure 1). It represents an oceanic core complex (OCC), where upper mantle peridotites and gabbroic rocks are exhumed along detachment faults (e.g., Blackman et al., 1998; Cann et al., 1997; Tucholke & Lin, 1994; Tucholke et al., 1998). Exhumation of mantle rocks at OCCs is probably caused by episodic and insufficient magma supply, and needed to counterbalance the spreading rate. The structure can be roughly subdivided into the central dome, where a large gabbroic body was discovered during IODP Expedition 304/305 drilling (Blackman et al., 2006; Ildefonse et al., 2007), an eastern hanging wall block formed by basalts (Blackman et al., 2002), and the southern wall which is to a large extent (~45%) made up of serpentinized peridotites, hosting the Lost City hydrothermal field (Früh-Green et al., 2018).

During International Ocean Discovery Program (IODP) Expedition 357, shallow (maximum depth 16.5 m) cores were drilled at nine sites along the top of the southern wall of the massif. Rock types range from sediments and basalts to serpentinized peridotites, talc-amphibole-chlorite schists and gabbros (Früh-Green et al., 2017, 2018). From a range of macroscopically different serpentinites (Rouméjon et al., 2018), we chose a suite of four compositionally simple and similar, but macroscopically variable samples for this study.

The samples are mainly composed of the serpentine mineral lizardite, with minor magnetite and chrysotile. Samples 71C3R1 (Site M0071C, Section 3.1, Interval 24–28 cm, 5.2 m below sea floor (mbsf)) and 71C9R1 (Site M0071C, Section 9R1, Interval 34–38 cm, 10 mbsf) originate from the western part of the southern wall of Atlantis Massif (see Figure 1). Their mesoscopic structure shows large (up to 1 cm) bastites. The third sample 76B5R1 (Site M0076B, Section 5.1, interval 63–67 cm, 7.4 mbsf) from the central part of the southern

wall, displays a (preferentially) orthogonal network of mesoscopic white veins. The fourth sample 68B4R1 (Site M0068B, Section 4.1, interval 87–90 cm, 4.9 mbsf) locates from further east on the southern wall. It has a dark green matrix with white and greenish veins.

3. Methods

3.1. Microstructure Analysis

The serpentinite microstructures were analyzed on thin sections using a petrographic microscope. Using the lambda retarder, oriented lizardite aggregates can be easily distinguished from optically isotropic (magenta) areas. Crystals with (0001) plane roughly aligned parallel to the retardation direction appear blue, those with (0001) plane perpendicular appear yellow, as long as (0001) remains within the thin-section plane. Micro X-ray fluorescence analysis was used to generate element maps of the thin sections. We used a Bruker Tornado M4 at the Mineralogy Department at Halle University with a Ag X-ray tube set to 50 kV and 600 μA, a step size between 15 and 20 μm, and a counting time of 24–35 ms/measurement point. Element maps of Al, Cr, Fe, Mg, Mn, and Si (Figures S1–S4) were used to segment phases using k-means cluster algorithm plugin in Fiji/ImageJ (Schindelin et al., 2012). The fabric strength was derived from the spatial arrangement of the magnetite phase, using the autocorrelation function (Panozzo Heilbronner, 1992), Jazy_ACF macro: https://github.com/kilir/Jazy_macros) on the segmented magnetite phase maps. Foliation strength is defined by $Fs = 1 - b/a$ in the range of 0–1, where a and b represent the long and short axis of an ellipse fitted to the ACF which is thresholded at a level representative of the area of the average magnetite fabric element (for details see Table S5). A Fs of 0 indicates an isotropic fabric, and larger values express an increasingly anisotropic, stronger fabric.

3.2. CPO Analysis

Samples for CPO analysis are cylinders with diameters of 15–20 mm. The synchrotron texture measurements were conducted at beamline ID22 at the European Synchrotron Radiation Facility (ESRF) in Grenoble (France) in transmission rotating the sample about the cylinder axis from 0° to 175° in 5° steps with 1 s exposure time. The resulting 36 images per measured sample position were collected with a Perkin Elmer image plate detector at a distance of 1401 mm to the sample. To overcome effects of potentially inadequate grain sampling, we measured on several positions along the cylinder axis of the samples. Beam size was set to ∼1 mm and beam energy to 70 keV. Data treatment and analysis was conducted using the Rietveld code MAUD (Material Analysis Using Diffraction, Lutterotti et al., 1997). Trigonal lizardite (Laurora et al., 2011) and magnetite (Fleet, 1981) were used as crystallographic input data. Serpentine in Rietveld analysis is represented only by lizardite, as chrysotile makes up less than 10% in all of the samples as constrained by light-optical microscopy.

In MAUD, the CPO is calculated using the EWIMV algorithm (Matthies & Vinel, 1982). The calculated Orientation Distribution Function (ODF, resolution: 15°) is imported into the Matlab toolbox MTEX (Hielscher & Schaeben, 2008, https://mtex-toolbox.github.io/) using parts of the Maud batch processing code by Daniel Savage (http://github.com/djm87/MAUD-TBP). In MTEX the orientations of the measurements from different sample positions are used to calculate a general sample ODF using a Dirichlet kernel estimation with a bandwidth of 7, corresponding to a halfwidth of 18°, as this is the most suitable kernel for physical properties calculations (Hielscher et al., 2015). The elastic properties are calculated as described by, for example, Mainprice et al. (2011) and Almqvist and Mainprice (2017) using the elasticity tensors from Auzende et al. (2006) as well as Tsuchiya (2013) (Table S6). CPO strength (texture index TI) is computed as the L2-norm of the ODF (Bunge, 1969). Displayed results of calculated velocities represent Hill averages. Voigt and Reuss averages can be found in Tables S7–S10.

4. Results

4.1. Microstructure

Sample 71C9R1 shows large bastites (up to 1 cm) embedded in a mesh microstructure (Figure 2a). Magnetite aggregates form discontinuous, vein-like structures which characterize a weak foliation ($Fs = 0.26$) as

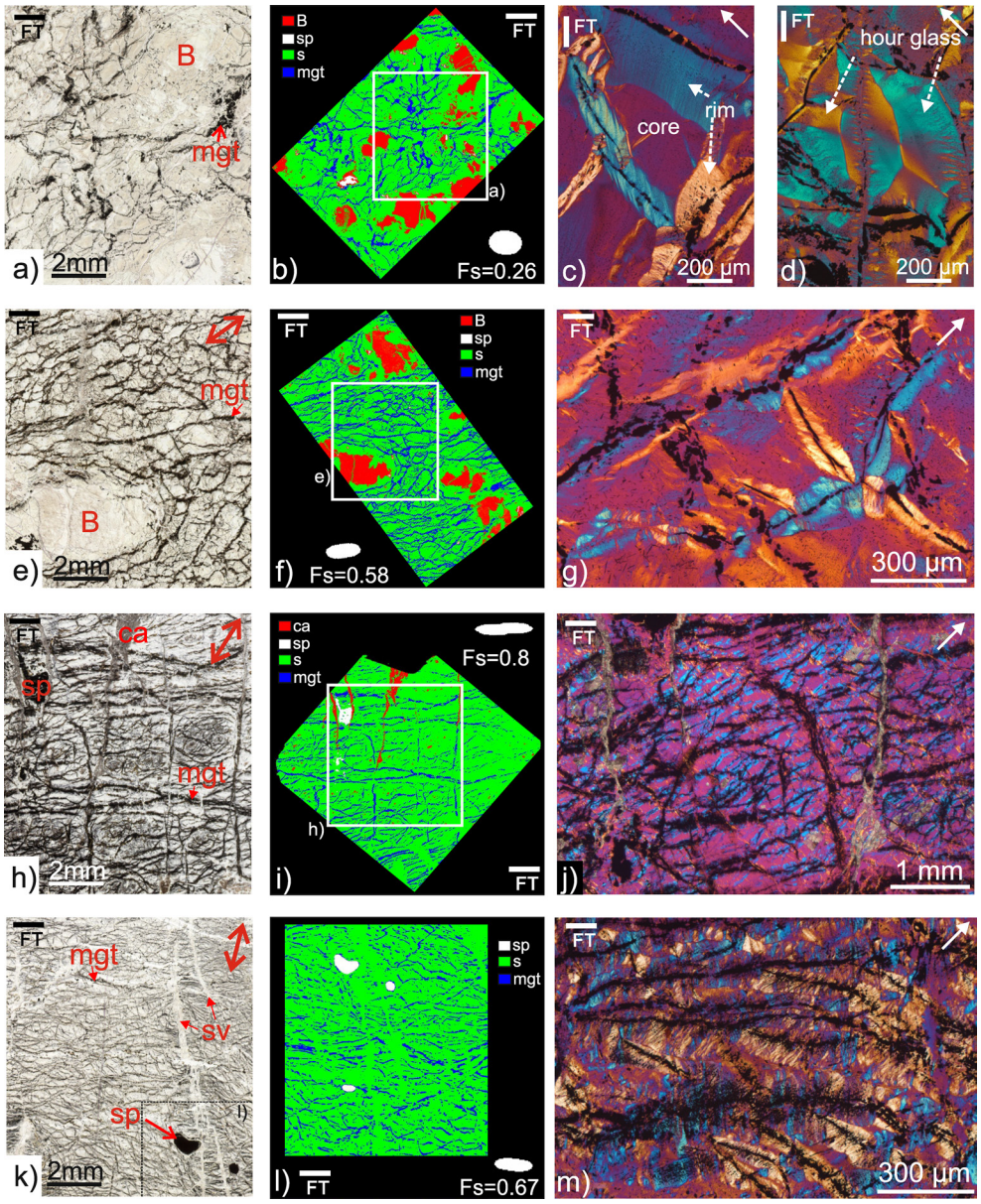

Figure 2. Microstructure images of sample (a)–(d) 71C9R1, (e)–(g) 71C3R1, (h)–(j) 76B5R1, and (k–m) 68B4R1. (a, e, h, k) Thin section scans at parallel polarized light. (b, f, i, l) Phase maps determined from segmentation of μXRF scans. Fabric strength FS determined from the thresholded autocorrelation function (white shapes) of segmented magnetite aggregates (blue). (c, d, g, j, m) Microscopic images with cross-polarized light and λ-retarder plate (White arrow shows retardation direction). (c) Mesh cell with isotropic (magenta) core, (d) mesh cell with hourglass structure, (g) mesh cells with rims and less clear defined cores, (j) closely spaced network of magnetite aggregates enclosing areas of isotropic and non-isotropic serpentine, (m) more disperse magnetite aggregates and mostly non-isotropic serpentine. FT, trace of foliation; b, bastite; mgt, magnetite; sp, cr-rich spinel; ca, calcite; sv, serpentine-filled veins. Red double-arrows: drill core axis if available.

determined from ACF analysis (Figure 2b). The serpentine mesh cells typically show rims of parallel oriented serpentine and optically isotropic cores (Figure 2c) or fully developed hourglass structures (Figure 2d).

In sample 71C3R1 bastites show a shape preferred orientation parallel to vein-like magnetite aggregates anastomosing around the bastites (Figure 2e) leading to a foliation strength *Fs* of 0.58 (Figure 2f). Serpentine mesh cells are still present but mesh cores are less clearly defined compared to sample 71C9R1 (Figure 2g).

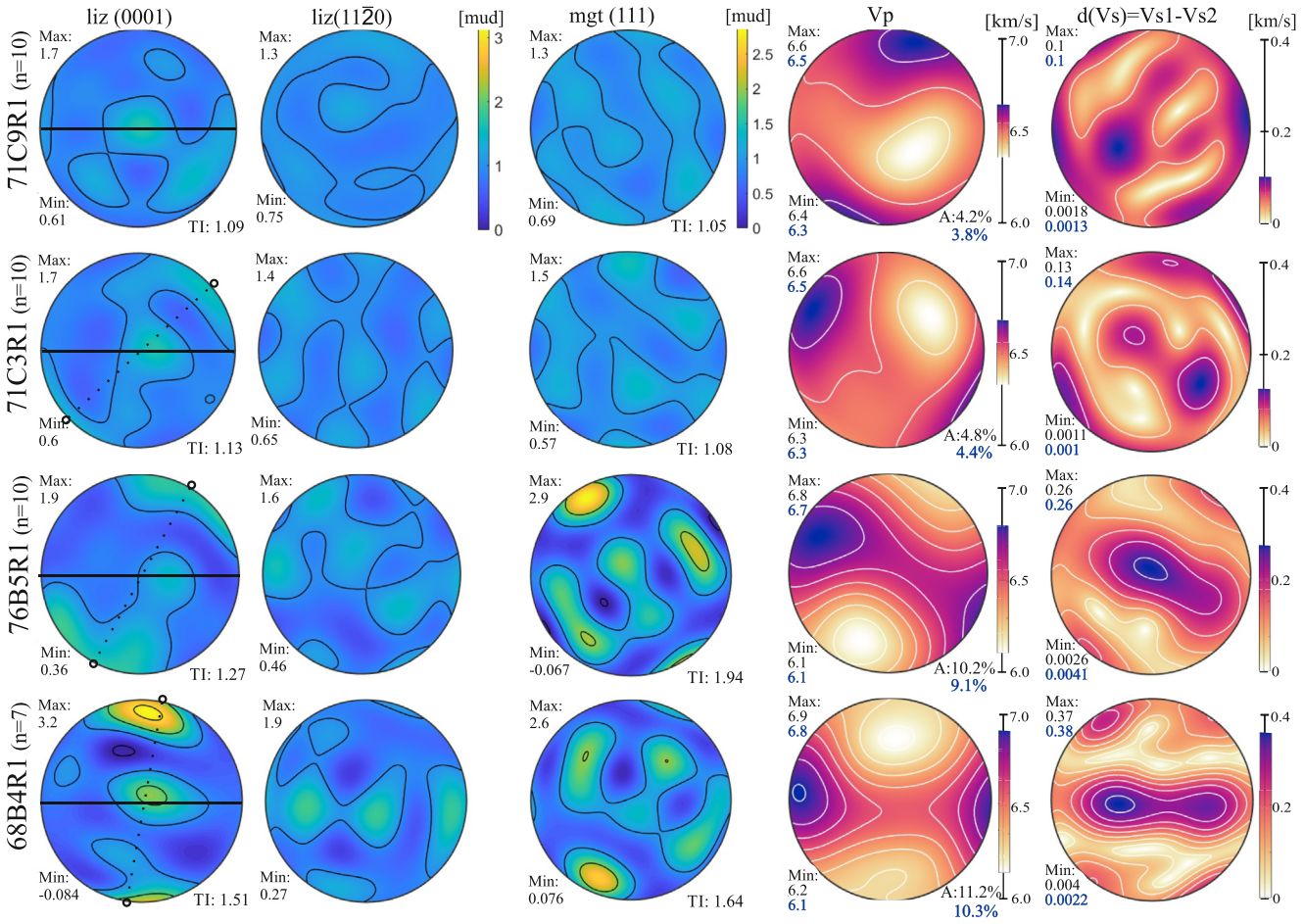

Figure 3. Recalculated pole figures for lizardite and magnetite (columns 1–3). Equal area, lower hemisphere projections. Maxima given in multiples of uniform distribution (mud), contour step 0.5. CPO strength TI is indicated below the corresponding pole figure. Foliation orientations are given as solid lines in the lizardite (0001) pole figures. Core axis directions (i.e., the vertical in nature) are shown in the same pole figures by dotted lines. In the first sample, core axis direction could not be reconstructed as sample was part of rubble found in the core liner. The number of stacked slices for each sample is given in brackets behind the sample name. Pole figures are projected in the same plane as the thin section images in Figure 2. Fourth column of plots shows calculated *Vp* anisotropies (Hill averages) using elasticity data from Auzende et al. (2006) (black letters) and Tsuchiya (2013) (blue letters), contour step 0.1, fifth column shows calculated shear wave splitting as difference of Vs1 and Vs2, contour step 0.05.

The strong foliation ($Fs = 0.8$) in sample 76B5R1 is characterized by parallel, continuous magnetite aggregates (Figures 2h and 2i), crosscut by calcite filled veins as well as further magnetite aggregates aligned at high angles to the foliation. Serpentine mesh cells are smaller and mostly show broad rims with a dominant orientation parallel to the retarder direction (blue) as well as areas of isotropic serpentine (magenta) (Figure 2j).

Sample 68B4R1 shows a ribbon-like microstructure (Figure 2k) with closely spaced, elongated magnetite aggregates sub-parallel to the mean trace of the foliation ($Fs = 0.67$) (Figure 2l). Cr-rich spinel is present in large, isolated grains. Serpentine cells show a higher occurrence of non-isotropic serpentine aggregates (Figure 2m), compared to all other samples. Large serpentine-filled veins crosscut the foliation fabric at high angles (Figure 2k).

4.2. CPO and Calculated Elastic Anisotropies

The lizardite (0001) pole figure in sample 71C9R1 (large bastites, no foliation) (Figure 3) shows a weak maximum with an intensity of ~1.7 multiples of uniform distribution (mud) and a texture index TI of 1.09. Sample 71C3R1 (large bastites, weak foliation) also shows a weak (~1.7 mud) maximum with TI = 1.13.

Magnetite (111) pole figures for both samples show weak, irregularly distributed maxima with 1.3–1.5 mud (TI = 1.05–1.08).

Lizardite in sample 76B5R1 (no bastites, regular foliation) shows a broad (0001) pole figure maximum with an intensity of ~1.9 mud/TI = 1.27 slightly inclined to the foliation normal. Sample 68B4R1 (no bastites, ribbon-like foliation) shows a strong (0001) maximum with an intensity of ~3.2 mud (TI = 1.51) which is normal to the foliation. The lizardite (11–20) pole figure is corresponding with a weak girdle distribution in the foliation plane. Magnetite pole figures for both samples show a pronounced maximum with ~2.6–2.9 mud/TI: 1.64–1.94 accompanied by some sub-maxima perpendicular to the main maximum.

The calculation of the seismic anisotropy is restricted to the lizardite CPO as magnetite is below 5% in the samples and does not exhibit a pronounced elastic anisotropy. Calculations show comparable results for both elasticity data sets used. Results show *Vp* anisotropies from 4.2% to 4.8% in the bastite-rich samples (71C9R1 & 71C3R1), and 10.2 (756B5R1) to 11.2% (68B4R1) *Vp* anisotropy for the bastite-free samples. Fast *Vp* directions for the latter two are sub-parallel or parallel, respectively, to the foliation and slow *Vp* directions are sub-parallel to the foliation normal. Simultaneously, shear wave splitting (d*Vs*) increases from 0.1 km/s for the bastite-rich samples to 0.37 km/s in the foliated samples and is strongest close or parallel to the foliation. Using the elasticity data for different pressures (see Table S10 and Figure S11) we observe a decrease in anisotropy from ~10% to <4% AVp at pressures >8 GPa.

5. Discussion

5.1. CPO-Forming Processes

Samples with bastites, typical equant mesh cells and a close to uniform CPO, are generally interpreted to be only weakly deformed (Viti & Mellini, 1998). Nevertheless, the spatial arrangement of magnetite aggregates shows a weak to medium planar anisotropy in one of those samples. We consider an alignment of previously randomly distributed magnetite grains and aggregates by straining of the entire volume without affecting the delicate serpentine microstructure as being unlikely. A viable mechanism allowing an alignment of magnetite aggregates without internally deforming the mesh cells would be dissolution-precipitation creep at serpentine-magnetite interfaces. Alternatively, the magnetite aggregates may have initially formed with the weak anisotropy during serpentinization, for example, due to anisotropic transport or veining.

Samples without bastites show a stronger magnetite foliation and also a stronger CPO. However, changes in the strength of the foliation and CPO cannot directly be correlated between the two samples. While one sample displays a higher foliation strength and a weaker CPO, the other one shows a weaker foliation strength and a stronger CPO (Figure 3). Both samples show microstructures typical for deformed serpentinites (Viti & Mellini, 1998; Viti et al., 2018). A relation between the CPO and the deformation shown by the microstructure seems likely. In sample 76B5R1, which exhibits a microstructure typical for deformed serpentinites with preferentially oriented lizardite (cf., Hirauchi et al., 2010; Viti et al., 2018), it might be speculated that the CPO is a result of frictional sliding or intracrystalline glide on the (001)-plane. The microstructure of sample 68B4R1 shows fewer and smaller domains of low-crystallinity serpentine and more oriented serpentine compared to the other samples, which might explain the stronger CPO. The origin of the higher amounts of more highly crystalline serpentine would usually be interpreted to be related to deformation by crystal plasticity (Hirauchi et al., 2010). However, the adjacency of magnetite seams and crystalline (textured) serpentine (Figure 2m) as well as an increase in crystallinity due to growth may also be interpreted in terms of CPO development that is unrelated to slip on (001). Textured serpentine adjacent to aligned magnetite aggregates could be related to (conjugate) fracturing and/or an oriented growth of serpentine. Based on the lack of evidence for pervasive straining by slip on (001), the origin of the textured serpentine may equally relate to growth or coarsening of serpentine along the aligned magnetite aggregates.

Based on the correlation of concurrent magnetite fabric and CPO development, we can conclude that samples with a pronounced magnetite foliation are likely to exhibit a non-random CPO. However, foliation strength seems not simply to be linked to CPO strength in low-grade metamorphic serpentinites. Other factors such as magnetite abundance, dependent on the fayalite component in the precursor olivine, and distribution may also play a role. The strength of the CPO in deformed serpentinites is highly dependent on the amount of stacks of more highly crystalline serpentine (Figure 2m).

5.2. Implications of Elastic Anisotropy

The textures of our samples show that the non- or weakly deformed serpentinites with a typical mesh cell structure behave more elastically isotropic, hence possess small seismic anisotropies. However, deformation causes a stronger texture and hence an increase in *Vp* anisotropy from ~4% in mesh cell samples, to >11% in foliated samples, as well as a 3 times higher shear wave splitting. As all samples are nearly 100% serpentinized, it is suggested that deformation of low-grade metamorphic serpentinites is a crucial factor for the development of seismic anisotropy. Higher-grade serpentinites in subduction settings are considered to be highly anisotropic (e.g., Jung, 2011). Our data shows that this can also be true for deformed low-grade metamorphic serpentinites.

In the bastite-free samples, we observe the orientation of the fast *Vp* direction parallel or sub-parallel to the foliation and the slow direction perpendicular to it. It follows that a typical seismic signature of a low-angle detachment, as present at oceanic OCC's would show fast sub-horizontal and slow sub-vertical *Vp* directions. The decrease in anisotropy with increasing pressure indicates that the identification of zones of deformation in serpentinites might be more challenging for greater depths than in shallower regions. For the Atlantis Massif OCC, we can show that the deformation is not restricted to one narrow localized zone, but more widely distributed through the serpentinites of the OCC.

6. Conclusion

Bulk rock CPO and microstructure of low-grade metamorphic serpentinites from the Atlantis Massif OCC show progressive deformation from original mesh to foliated structures. From the calculated elastic anisotropy, we show that the seismic anisotropy in serpentinites significantly differs in deformed and undeformed samples and may therefore be used to identify shear zones, for example, detachment faults, from seismic imaging of the hydrated upper mantle, and especially of OCCs, presuming sufficient extent of the anisotropic area.

Data Availability Statement

Data used in this study can be found at https://doi.org/10.5281/zenodo.4540184.

Acknowledgments
We are grateful for the enthusiasm of all members of the IODP Expedition 357 Scientific Party, their great collaborative work at sea and in the Bremen Core Repository, and their determination to make the expedition a success. Synchrotron texture measurements were conducted at the European Synchrotron Radiation Facility (ESRF) in Grenoble, France. We acknowledge the great support offered by Andy Fitch and his group at ESRF ID22. We appreciate the suggestions of two anonymous reviewers, which helped to improve the manuscript. This study was funded by an award of Deutsche Forschungsgemeinschaft (DFG) Project BE1041/34-1 to J. H. Behrmann.

References

Almqvist, B. S. G., & Mainprice, D. (2017). Seismic properties and anisotropy of the continental crust: Predictions based on mineral texture and rock microstructure. *Reviews of Geophysics*, *55*, 367–433. https://doi.org/10.1002/2016RG000552

Amiguet, E., Reynard, B., Caracas, R., Van de Moortèle, B., Hilairet, N., & Wang, Y. (2012). Creep of phyllosilicates at the onset of plate tectonics. *Earth and Planetary Science Letters*, *345–348*, 142–150. https://doi.org/10.1016/j.epsl.2012.06.033

Amiguet, E., Van De Moortèle, B., Cordier, P., Hilairet, N., & Reynard, B. (2014). Deformation mechanisms and rheology of serpentines in experiments and in nature. *Journal of Geophysical Research: Solid Earth*, *119*, 4640–4655. https://doi.org/10.1002/2013JB010791

Aumento, F., & Loubat, H. (1971). The Mid-Atlantic Ridge Near 45°N. XVI. Serpentinized ultramafic intrusions. *Canadian Journal of Earth Sciences*, *8*, 631–663. https://doi.org/10.1139/e71-062

Auzende, A.-L., Pellenq, R. J.-M., Devouard, B., Baronnet, A., & Grauby, O. (2006). Atomistic calculations of structural and elastic properties of serpentine minerals: The case of lizardite. *Physics and Chemistry of Minerals*, *33*, 266–275. https://doi.org/10.1007/s00269-006-0078-x

Bezacier, L., Reynard, B., Bass, J. D., Sanchez-Valle, C., & Van de Moortèle, B. (2010). Elasticity of antigorite, seismic detection of serpentinites, and anisotropy in subduction zones. *Earth and Planetary Science Letters*, *289*, 198–208. https://doi.org/10.1016/j.epsl.2009.11.009

Blackman, D. K., Cann, J. R., Janssen, B., & Smith, D. K. (1998). Origin of extensional core complexes: Evidence from the Mid-Atlantic Ridge at Atlantis Fracture Zone. *Journal of Geophysical Research*, *103*, 21315–21333. https://doi.org/10.1029/98JB01756

Blackman, D. K., Ildefonse, B., John, B. E., Ohara, Y., Miller, D. J., MacLeod, C. J., & The Expedition 304/305 Scientists. (2006). Proceedings of the Integrated Ocean Drilling Program Volume 304/305. College Station, TX.

Blackman, D. K., Karson, J. A., Kelley, D. S., Cann, J. R., Früh-Green, G. L., Gee, J. S., et al. (2002). Geology of the Atlantis Massif (Mid-Atlantic Ridge, 30° N): Implications for the evolution of an ultramafic oceanic core complex. *Marine Geophysical Researches*, *23*, 443–469. https://doi.org/10.1023/B:MARI.0000018232.14085.75

Boschi, C., Früh-Green, G. L., Delacour, A., Karson, J. A., & Kelley, D. S. (2006). Mass transfer and fluid flow during detachment faulting and development of an oceanic core complex, Atlantis Massif (MAR 30°N). *Geochemistry, Geophysics, Geosystems*, *7*, Q01004. https://doi.org/10.1029/2005GC001074

Boudier, F., Baronnet, A., & Mainprice, D. (2010). Serpentine mineral replacements of natural olivine and their seismic implications: Oceanic lizardite versus subduction-related antigorite. *Journal of Petrology*, *51*, 495–512. https://doi.org/10.1093/petrology/egp049

Bunge, H. J. (1969). *Mathematische Methoden der Texturanalyse*. Berlin: Akademie-Verlag.

Cann, J. R., Blackman, D. K., Smith, D. K., McAllister, E., Janssen, B., Mello, S., et al. (1997). Corrugated slip surfaces formed at ridge-transform intersections on the Mid-Atlantic ridge. *Nature*, *385*, 329–332. https://doi.org/10.1038/385329a0

Escartín, J., Hirth, G., & Evans, B. (1997). Nondilatant brittle deformation of serpentinites: Implications for Mohr-Coulomb theory and the strength of faults. *Journal of Geophysical Research*, *102*(B2), 2897–2913. https://doi.org/10.1029/96JB02792

Escartín, J., Hirth, G., & Evans, B. (2001). Strength of slightly serpentinized peridotites: Implications for the tectonics of oceanic lithosphere. *Geology*, *29*, 1023–1026. https://doi.org/10.1130/0091-7613(2001)029<1023:SOSSPI>2.0.CO;2

Evans, B. W. (2004). The serpentinite multisystem revisited: Chrysotile is metastable. *International Geology Review*, *46*, 479–506. https://doi.org/10.2747/0020-6814.46.6.479

Fleet, M. E. (1981). The structure of magnetite. *Acta Crystallographica Section B*, *37*(4), 917–920. https://doi.org/10.1107/S0567740881004597

Früh-Green, G. L., Orcutt, B. N., Green, S. L., Cotterill, C., & The E. 357 Scientists. (2017), Proceedings of the International Ocean Discovery Program Volume 357 Atlantis Massif Serpentinization and Life. College Station, TX.

Früh-Green, G. L., Orcutt, B. N., Rouméjon, S., Lilley, M. D., Morono, Y., Cotterill, C., et al. (2018). Magmatism, serpentinization and life: Insights through drilling the Atlantis Massif (IODP Expedition 357). *Lithos*, *323*, 137–155. https://doi.org/10.1016/j.lithos.2018.09.012

Guillot, S., Schwartz, S., Reynard, B., Agard, P., & Prigent, C. (2015). Tectonic significance of serpentinites. *Tectonophysics*, *646*, 1–19. https://doi.org/10.1016/j.tecto.2015.01.020

Hielscher, R., Mainprice, D., & Schaeben, H. (2015). Material behavior: Texture and anisotropy. In W. Freeden, M. Zuhair Nashed, & T. Sonar (Eds.), *Handbook of geomathematics* (pp. 2149–2188). Berlin: Springer. https://doi.org/10.1007/978-3-642-54551-1_33

Hielscher, R., & Schaeben, H. (2008). A novel pole figure inversion method: Specification of the MTEX algorithm. *Journal of Applied Crystallography*, *41*, 1024–1037. https://doi.org/10.1107/S0021889808030112

Hirauchi, K.-I., Katayama, I., Uehara, S., Miyahara, M., & Takai, Y. (2010). Inhibition of subduction thrust earthquakes by low-temperature plastic flow in serpentine. *Earth and Planetary Science Letters*, *295*, 349–357. https://doi.org/10.1016/j.epsl.2010.04.007

Ildefonse, B., Blackman, D. K., John, B. E., Ohara, Y., Miller, D. J., & MacLeod, C. J. (2007). Oceanic core complexes and crustal accretion at slow-spreading ridges. *Geology*, *35*, 623–626. https://doi.org/10.1130/G23531A.1

Jung, H. (2011). Seismic anisotropy produced by serpentine in mantle wedge. *Earth and Planetary Science Letters*, *307*, 535–543. https://doi.org/10.1016/j.epsl.2011.05.041

Lau, K. W. H., Louden, K. E., Deemer, S., Hall, J., Hopper, J. R., Tucholke, B. E., et al. (2006). Crustal structure across the Grand Banks – Newfoundland Basin Continental Margin – II. Results from a seismic reflection profile. *Geophysical Journal International*, *167*, 157–170. https://doi.org/10.1111/j.1365-246X.2006.02989.x

Laurora, A., Brigatti, M. F., Malferrari, D., Galli, E., Rossi, A., & Ferrari, M. (2011). The crystal chemistry of lizardite-1T from Northern Apennines ophiolites near Modena, Italy. *The Canadian Mineralogist*, *49*, 1045–1054. https://doi.org/10.3749/canmin.49.4.1045

Lutterotti, L., Matthies, S., Wenk, H.-R., Schultz, A. S., & Richardson, J. W. (1997). Combined texture and structure analysis of deformed limestone from time-of-flight neutron diffraction spectra. *Journal of Applied Physics*, *81*, 594–600. https://doi.org/10.1063/1.364220

Mainprice, D., Hielscher, R., & Schaeben, H. (2011). Calculating anisotropic physical properties from texture data using the MTEX open-source package. *Geological Society, London, Special Publications*, *360*, 175–192. https://doi.org/10.1144/SP360.10

Matthies, S., & Vinel, G. W. (1982). On the reproduction of the orientation distribution function of texturized samples from reduced pole figures using the conception of a conditional ghost correction. *physica status solidi (b)*, *112*, K111–K114. https://doi.org/10.1002/pssb.2221120254

Moore, D. E., & Rymer, M. J. (2007). Talc-bearing serpentinite and the creeping section of the San Andreas fault. *Nature*, *448*, 795–797. https://doi.org/10.1038/nature06064

Panozzo Heilbronner, R. (1992). The autocorrelation function: An image processing tool for fabric analysis. *Tectonophysics*, *212*, 351–370. https://doi.org/10.1016/0040-1951(92)90300-u

Raleigh, C. B., & Paterson, M. S. (1965). Experimental deformation of serpentinite and its tectonic implications. *Journal of Geophysical Research*, *70*(16), 3965–3985. https://doi.org/10.1029/JZ070i016p03965

Rouméjon, S., Früh-Green, G. L., Orcutt, B. N., & The Expedition 357 Science Party. (2018). Alteration heterogeneities in peridotites exhumed on the southern wall of the Atlantis Massif (IODP Expedition 357). *Journal of Petrology*, *59*(7), 1329–1358. https://doi.org/10.1093/petrology/egy065/5042903

Schindelin, J., Arganda-Carreras, I., Frise, E., Kaynig, V., Longair, M., Pietzsch, T., et al. (2012). Fiji: An open-source platform for biological-image analysis. *Nature Methods*, *9*(7), 676–682. https://doi.org/10.1038/nmeth.2019

Solarino, S., Malusà, M. G., Eva, E., Guillot, S., Paul, A., Schwartz, S., et al. (2018). Mantle wedge exhumation beneath the Dora-Maira (U) HP dome unravelled by local earthquake tomography (Western Alps). *Lithos*, *296*, 623–636. https://doi.org/10.1016/j.lithos.2017.11.035

Sutra, E., Manatschal, G., Mohn, G., & Unternehr, P. (2013). Quantification and restoration of extensional deformation along the Western Iberia and Newfoundland rifted margins. *Geochemistry, Geophysics, Geosystems*, *14*(8), 2575–2597. https://doi.org/10.1002/ggge.20135

Tsuchiya, J. (2013). A first-principles calculation of the elastic and vibrational anomalies of lizardite under pressure. *American Mineralogist*, *98*(11–12), 2046–2052. https://doi.org/10.2138/am.2013.4369

Tucholke, B. E., & Lin, J. (1994). A geological model for the structure of ridge segments in slow spreading ocean crust. *Journal of Geophysical Research*, *99*, 11937–11958. https://doi.org/10.1029/94JB00338

Tucholke, B. E., Lin, J., & Kleinrock, C. (1998). Megamullions and mullion structure defining oceanic metamorphic core complexes on the Mid-Atlantic Ridge. *Journal of Geophysical Research*, *103*, 9857–9866. https://doi.org/10.1029/98JB00167

Viti, C., Collettini, C., Tesei, T., Tarling, M. S., & Smith, S. A. F. (2018). Deformation processes, textural evolution and weakening in retrograde serpentinites. *Minerals*, *8*, 241. https://doi.org/10.3390/min8060241

Viti, C., & Mellini, M. (1998). Mesh textures and bastites in the Elba retrograde serpentinites. *European Journal of Mineralogy*, *10*, 1341–1359.

Wicks, F. J., & Whittaker, E. J. W. (1977). Serpentine textures and serpentinization. *The Canadian Mineralogist*, *15*, 459–488.

Zhao, L., Malusà, M. G., Yuan, H., Paul, A., Guillot, S., Lu, Y., et al. (2020). Evidence for a serpentinized plate interface favouring continental subduction. *Nature Communications*, *11*(1), 1–8. https://doi.org/10.1038/s41467-020-15904-7